Exotic phases of matter in quantum magnets

A tensor networks tale

Niesen, I.A.

Publication date
2018
Document Version
Other version
License
Other

CHAPTER 4

The triangular lattice bilinear-biquadratic Heisenberg model

Making use of infinite projected entangled pair states, we investigate the ground state phase diagram of the nearest-neighbor spin-1 bilinear-biquadratic Heisenberg model on the triangular lattice. In agreement with previous studies, we find the ferromagnetic, 120° magnetically ordered, ferroquadrupolar and antiferroquadrupolar phases, and confirm that all corresponding phase transitions are first order. Moreover, we provide an accurate estimate of the location of the ferroquadrupolar to 120° magnetically ordered phase transition, thereby fully establishing the phase diagram. Also, we do not encounter any signs of the existence of a quantum paramagnetic phase. In particular, contrary to the equivalent square lattice model, we demonstrate that on the triangular lattice the one-dimensional Haldane phase does not *reach all the way up to the two-dimensional limit.*

The contents of this chapter are based on Ref. [3].

4.1 Introduction

Geometric frustration in strongly correlated materials can cause even relatively simple systems to develop unexpected types of order. For magnetic materials, the archetypal example of a geometrically frustrated system is the triangular lattice Heisenberg antiferromagnet. In 1973, Anderson [13] proposed that the spin-1/2

triangular antiferromagnet has a ground state consisting of resonating valence bonds, also called a quantum spin liquid. However, it was later shown numerically [35, 36] that the ground state is ordered instead and displays 120-degree magnetic order.

In this chapter, we focus on the two-dimensional triangular lattice spin-1 Heisenberg model with additional biquadratic coupling. As in the previous chapter, it is defined by the following Hamiltonian

$$H = \sum_{\langle i,j \rangle} \cos(\theta)\, \boldsymbol{S}_i \cdot \boldsymbol{S}_j + \sin(\theta)\, (\boldsymbol{S}_i \cdot \boldsymbol{S}_j)^2 , \tag{4.1}$$

where the sum goes over all nearest neighbors, $\boldsymbol{S}_i = (S_i^x, S_i^y, S_i^z)$ is the vector of spin-matrices for the spin-1 particle on site i, and $\theta \in [0, 2\pi)$ determines the strength of the biquadratic term relative to the bilinear term. The difference with the model investigated in the previous chapter is that the underlying lattice has a different structure and a higher coordination number (six instead of four), which will turn out to alter the ground state phase diagram significantly.

The triangular lattice spin-1 BBH model gained attention recently because it was suggested that both its antiferroquadrupolar [154, 157, 178] and ferroquadrupolar [156,179] ground state phases could give a possible explanation for the unusual behavior [161, 180, 181] of $NiGa_2S_4$. Moreover, Cheng et al. [162] found spin-liquid-like behavior of the $6H$-B phase of the two-dimensional triangular magnet $Ba_3NiSb_2O_9$ [163, 182], for which Serbyn et al. [183] proposed a candidate spin-liquid ground state that within the mean-field approximation was supposed to be a ground state the triangular spin-1 BBH model with additional single-ion anisotropy. However, a further investigation by Bieri et al. [159] demonstrated that the the spin-liquid state found by Serbyn et al. [183] turned out *not* to be the lowest energy state of the triangular spin-1 BBH model with single ion anisotropy.

Additionally, at $\theta = \pi/4$, the BBH model is equivalent to the SU(3) Heisenberg model, which could potentially be simulated using cold atoms trapped in an optical lattice [164–167, 184–187]. Besides, as the most general spin-1 lattice-translation, lattice-rotation and spin-rotation-symmetric Hamiltonian with nearest-neighbor interactions, the BBH Hamiltonian is interesting in its own right from a theoretical point of view.

Moreover, in our study of the spin-1 BBH model on the square lattice presented in Chapter 3, we found the occurrence of a quantum paramagnetic phase in between the antiferromagnetic and 120° magnetically ordered phases, and we were able to show that this phase can be adiabatically connected to the one-dimensional Haldane phase of decoupled spin-1 chains. In addition, we also encountered a partially magnetic partially nematic phase in between the antiferroquadrupolar and ferromagnetic phases. Both discoveries raise the question whether any of the above phenomena also manifest themselves on the experimentally more relevant triangular lattice.

Finally, it should be noted that the spin-1 BBH model on the triangular lattice is very challenging to study from a numerical perspective, as it suffers from the negative sign problem. Previous studies—summarized in Section 4.3—are either based on approximate methods, or involve exact diagonalization on small systems; however, a complete and systematic study is still lacking.

In this chapter, we use the methods explained in Chapter 2 to map the entire ground state phase diagram of the triangular lattice spin-1 BBH model—displayed in Fig. 4.1. In agreement with previous studies, we find the ferromagnetic (FM), ferroquadrupolar (FQ), 120° antiferromagnetically ordered (AFM3)[1] and antiferroquadrupolar (AFQ) phases and obtain an accurate estimate of the location of the FQ to AFM3 transition—which we predict to occur at $\theta_c = 1.873\pi \pm 0.007\pi$—thereby fully establishing the phase diagram.

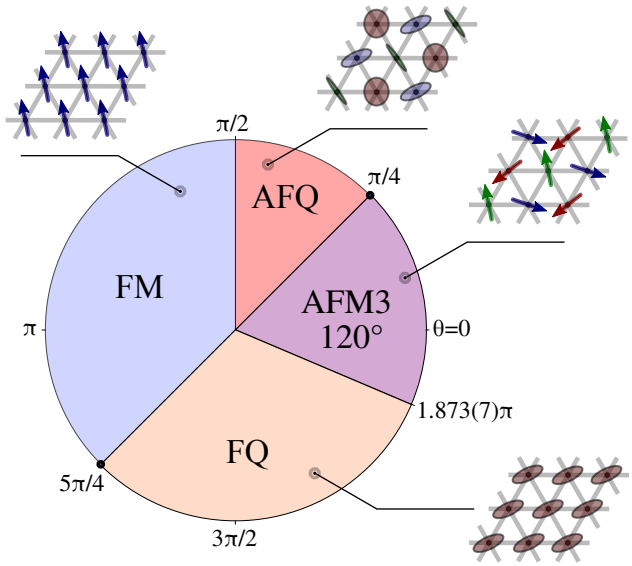

Figure 4.1: *The iPEPS ground state phase diagram. In anti-clockwise order starting at $\theta = 0$, we have the 120 degree magnetically ordered (AFM3), antiferroquadrupolar (AFQ), ferromagnetic (FM) and ferroquadrupolar (FQ) phases. The SU(3)-symmetric points at $\theta = \pi/4$ and $5\pi/4$ are labeled by black dots.*

Motivated by our findings for the corresponding square lattice model presented in Chapter 3, we also investigate the anisotropic triangular lattice spin-1 BBH model for $\theta \in (-\pi/4, \pi/4)$. We show that, on the triangular lattice, the one-dimensional

[1] Recall that the "3" indicates three-sublattice order: it is used to differentiate 120° magnetic order (AFM3) from ordinary antiferromagnetic order (AFM), the latter of which displays a two-sublattice pattern.

Haldane phase does *not* reach up to the two-dimensional isotropic model—albeit that it *does* extend far from the one-dimensional limit. In addition, the triangular-lattice equivalent of the partially magnetic partially nematic phase found on the square lattice is shown to *not* be present in the ground state phase diagram of the triangular lattice spin-1 BBH model.

This chapter is organized as follows. We set the stage by discussing previous work that has been done on the triangular lattice spin-1 BBH model in Section 4.3, and identify possible points of interest. After benchmarking the triangular lattice algorithm in Section 4.4, we then present our results concerning the ground state phase diagrams of the isotropic and anisotropic triangular lattice spin-1 BBH models in Section 4.5. Finally, we discuss our findings in Section 4.6.

4.2 Model preliminaries

Recall that, as explained in Section 3.2, the Hamiltonian in Eq.(4.1) can be rewritten in terms of the quadrupolar vectors $\boldsymbol{Q}_i$—see Eq. (3.2)—which yields

$$H = \sum_{\langle i,j \rangle} J_S(\theta)\, \boldsymbol{S}_i \cdot \boldsymbol{S}_j + J_Q(\theta)\, \boldsymbol{Q}_i \cdot \boldsymbol{Q}_j \tag{4.2}$$

up to an irrelevant θ-dependent constant of $4\sin(\theta)/3$. The spin and quadrupolar coupling constants given by $J_S(\theta) = \cos(\theta) - \sin(\theta)/2$ and $J_Q(\theta) = \sin(\theta)/2$.

In addition to separating the dipolar and quadrupolar terms—related to magnetic and (spin) *nematic* order respectively—writing the Hamiltonian in terms of the spin and quadrupole operators as in Eq. (4.2) has the additional advantage that the points of enhanced SU(3)-symmetry are made explicit, which in the case of the tripartite[2] triangular lattice are only those for which $J_S = J_Q$, i.e. $\theta = \pi/4$ and $5\pi/4$.

Technically, quadrupolar order is described by the spectrum of the Q-matrix. Since $\mathrm{tr}(Q) = 0$, the spectrum is fully determined by two matrix invariants, for which there are many possible choices, such as: two out of three eigenvalues, or, the invariants $II_Q = -\frac{1}{2}\mathrm{tr}(Q)^2$ and $III_Q = \det(Q)$ used in the previous chapter. However, when we are searching for jumps in the Q-matrix spectrum that signify a (first order) phase transition, finding a jump in just one matrix invariant is sufficient. An obvious choice is the vector norm $|\boldsymbol{Q}| = \sqrt{\boldsymbol{Q} \cdot \boldsymbol{Q}}$, which [170] is also equal to ($1/\sqrt{2}$ times) the Frobenius norm $\sqrt{\mathrm{tr}(Q^\dagger Q)}$ of the Q-matrix. We will refer to this norm as the *Q-norm* for short.

[2] Taking the antifundamental representation on a sublattice does not cancel the extra minus sign on all bonds at $\theta = \pm\pi/2$ as it does on the square lattice—see Section 3.2.2.

4.3 Previous studies

Spin-1 BBH models have been extensively studied throughout the years. Of relevance to our investigation of the triangular lattice BBH model in particular, is the pioneering construction by Affleck, Kennedy, Lieb and Takasaki [188] of an exact ground state of the spin-1 BBH chain at $\theta = \arctan(1/3)$ in the middle of the Haldane phase [133, 134]. In dimensions higher than one, Papanicolaou [152] was the first to develop a more flexible form of spin-wave theory that was readily applicable to spin-1 BBH models on bipartite lattices. However, it was not until 2005 that a discovery of a low temperature spin-disordered state in the triangular magnet $NiGa_2S_4$ by Nakatsuji et al. [161, 180]) sparked a surge of increased interest in the spin-1 BBH model on the two-dimensional triangular lattice, initializing a series of vibrant discussions [154–156] in 2006 on the nature of this new-found spin-disordered state.

In order to introduce some terminology, let us us first discuss the already very rich product ground state phase diagram of the triangular lattice spin-1 BBH model—shown in Fig. 4.2—computed by Läuchli et al. [155] (to be discussed below) assuming a tripartite site-factorized product state ansatz for the ground state. In addition to the magnetized 120° antiferromagnetically ordered (AFM3) and fer-

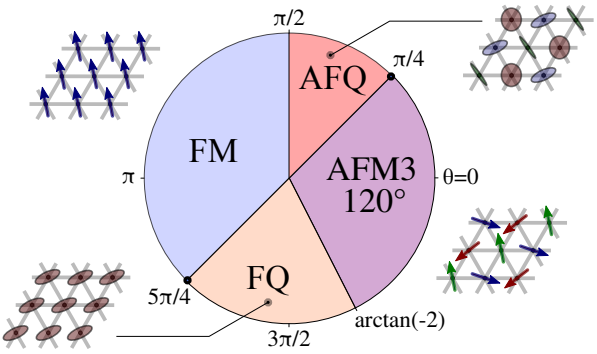

Figure 4.2: *The product ground state phase diagram. The FQ to AFM3 phase transition occurs at* $\Theta_c^{MF} = \arctan(-2) \approx 1.648\pi$ *(Läuchli et al. [155]).*

romagnetic (FM) phases, Fig. 4.2 also contains the nematic ferroquadrupolar (FQ) and antiferroquadrupolar (AFQ) phases.

Recall from Sections 3.2 and 3.3 that product states in the ferroquadrupolar phase have directors on neighboring sites align in the same direction, whereas states in the antiferroquadrupolar phase have neighboring directors align in mutually perpendicular directions—e.g. in the x, y and z-directions—assuming a three-sublattice pattern. The quadrupolar states are pictured by discs in Fig.'s 4.1 and 4.2 representing their planes of spin fluctuations.

Following the above-mentioned discovery of Nakatsuji et al. [161], a 2006 study by Tsunetsugu and Arikawa [154]—followed up by a 2007 paper [157] of the same authors—investigated the AFQ phase of the triangular lattice spin-1 BBH model by means of bosonic excitations on top of the product ground state. They proposed that the AFQ phase could explain many features of the new-found spin disordered state in $NiGa_2S_4$.

Barely eight days after Tsunetsugu and Arikawa [154] submitted their 2006 work, Läuchli et al. [155] handed in a paper (containing also the product ground state phase diagram in Fig. 4.2) in which they performed exact diagonalization of systems of up to 21 sites to compute spin and quadrupolar structure factors, from which they determined that the mean-field critical parameter value $\Theta_c^{MF} = \arctan(-2)$ that separates the FQ from the AFM3 phase gets renormalized to $\Theta_c^{ED} \approx -0.11\pi$. Moreover, Läuchli et al. also investigated the non-zero field phase diagram, and used flavor-wave theory based on Papanicolaou's method [152] to investigate the spin-wave excitation spectrum. The most surprising feature that Läuchli et al. find is the occurrence of a $m = 2/3$ magnetization plateau in the AFQ phase without the occurrence of a $m = 1/3$ magnetization plateau (something that is unlikely to occur for purely magnetic states because of the lower commensurability of the latter), and they consider this a characteristic of the AFQ phase.

A mere three days after Läuchli et al. submitted their work, Bhattacharjee et al. [156] submitted a paper that, contrary to Tsunetsugu and Arikawa's proposition [154], explores the possibility that the new-found spin-disordered state in $NiGa_2S_4$ is actually of ferroquadrupolar type. In 2009, Stoudenmire et al. [179] investigated the $T > 0$ behavior of the spin-1 triangular BBH model augmented with third-neighbor interactions using classical Monte Carlo, and argued that the quadrupolar correlations are actually more robust than the ferroquadrupolar ground state itself, the former of which are identifiable by a twin-peak structure in the specific heat. A 2010 paper by Nakatsuji et al. [181] that revisited the case of $NiGa_2S_4$ mentions, among other things, that the FQ phase is indeed a more likely candidate for the ground state than the AFQ phase because of the appearance of a $m = 1/3$ magnetization plateau and the absence of a superlattice peak compatible with the AFQ unit cell.

In 2012, Kaul [189] performed quantum Monte Carlo simulations at the pure biquadratic point $\theta = -\pi/2$, confirming that the the ground state is nematic, and provided accurate estimates of parameters such as the specific heat and the susceptibility. Moreno-Cardoner et al. [190] studied the spin-1 BBH model with uniaxial anisotropy field in 2014 using a cluster mean-field approach (CMF). In the same year, Pires [191] calculated the dynamical quadrupole structure factor in the FQ phase using the SU(3) Schwinger boson formalism, and in 2015, Völl et al. [192], studied the dynamical spin and quadrupolar structure factors in the region $\theta \in [\pi, 3\pi/2]$ encompassing parts of the FM and FQ phases by means of

quantum Monte Carlo.

As discussed in Chapter 3, we conducted an iPEPS study of the spin-1 BBH model on the two-dimensional square lattice, which yielded the occurrence of two additional phases on top of those present in the product ground state phase diagram. In particular, we found that in between the ordinary antiferromagnetic (AFM) and 120° magnetically ordered (AFM3) phases, a quantum paramagnetic phase arises that is characterized by the fact that it preserves spin-rotation and lattice-translation symmetry while breaking lattice-rotation symmetry due to energy differences between the x and y-bonds. Moreover, by continuously shrinking all high energy bond couplings to zero, the quantum paramagnetic phase turned out to be adiabatically connected to the Haldane phase of decoupled spin-1 chains, and can thus be viewed as a two-dimensional extension of the latter.

In addition to the Haldane phase, on the square lattice we also encountered the $m = 1/2$ partially magnetic partially nematic phase—a phase that was predicted to appear only in the presence of an external magnetic field by Tóth et al. [158]—and found that this phase is also present in the zero-field phase diagram.

Motivated by the above discoveries, we shall investigate the region $-\pi/4 < \theta < \pi/4$ where the Haldane phase occurs in the one-dimensional BBH chain, and keep an eye out for possible intermediate quantum paramagnetic phases. Moreover, in light of the characteristic $m = 2/3$ magnetization plateau in the AFQ phase in the presence external magnetic field [155], we will also investigate the possibility that the $m = 2/3$ phase extends to the zero-field phase diagram of the triangular lattice spin-1 BBH model.

4.4 SU(3)-symmetric point benchmark

Before we proceed, let us benchmark the triangular lattice simple, full and variational update algorithms at the SU(3)-symmetric point $\theta = \pi/4$ by comparing to a previous study of the SU(3)-Heisenberg model by Bauer et al. [169]. We make use of the additional symmetries of the Hamiltonian to push the bond dimension to $D = 16$ for the simple update, and $D = 12$ for the full and variational updates. (See Refs. [112, 113] on how to implement global abelian symmetries within the tensor network formalism.) The resulting energies per site are shown in Fig. 4.3.

Fig. 4.3 shows that the full and variational update both give a visible improvement over the simple update. This reflects the fact that the former two both use the full environment at each optimization step, whereas the simple update only uses an approximate environment—making it computationally cheaper.

Because the ansatz used for the ground state is variational, each iPEPS energy computed is higher than or equal to the true ground state energy. Therefore, the lowest finite-D energy obtained—in this case given by the $D = 12$ variational

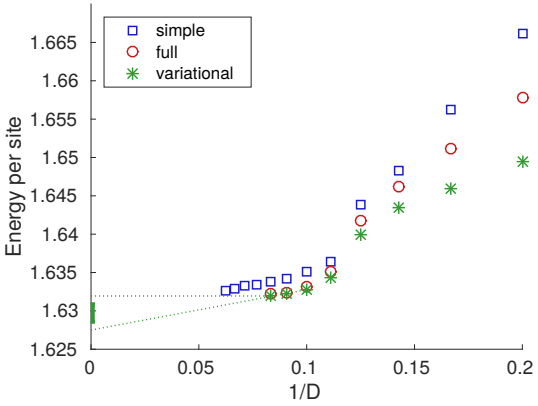

Figure 4.3: *Energy per site at the SU(3) point $\theta = \pi/4$ for the simple, full and variational update. The simulations make use of the SU(3) symmetry of the ground state and can therefore be ran at higher bond dimension than usual. We take the midpoint of the ends of the two dotted lines to be the $D \to \infty$ extrapolated energy per site (see main text).*

update simulation (shown in green) with an energy of $E^{\text{var}}_{D=12} = 1.632$—serves as an upper bound for the true ground state energy. Since increasing D introduces more variational parameters in the iPEPS, the energy of the iPEPS decreases as D increases. However, the behavior of the energy of an iPEPS is typically such that the energy as a function of $1/D$ curve flattens out as D increases. Thus, a lower bound for the true ground state energy can be obtained by drawing a straight line through the last few high-D data points (depicted by the lowest dotted green line in Fig. 4.3) and extrapolating it to $D \to \infty$. We shall take the average of the lowest obtained finite-D energy ($E^{\text{var}}_{D=12}$) and the straight-line extrapolated energy through the last few data points as our estimate for the true ground state energy, which in this case yields $E^{\text{var}}_{D\to\infty} = 1.630$. Because the above-mentioned bounds are loose bounds, for our estimate of the error we shall take half of the difference between the lowest obtained energy and the straight-line extrapolated energy, resulting in an extrapolated energy of $E^{\text{var}}_{D\to\infty} = 1.630(1)$. The error bar is depicted by the thin green slab on the y-axis in Fig. 4.3[3].

Contrasted to the result obtained by Bauer et al. [169] of $E^{\text{previous}}_{D\to\infty} = 1.633(14)$, we can conclude that our result is not only slightly lower in energy, but also more accurate; in part because we can go to higher bond dimension, but also due to algorithmic improvement. Indeed, the lowest finite-D energy obtained by Bauer et al. is a $D = 10$ simulation with an energy of $E^{\text{previous}}_{D=10} = 1.646$, which is higher

[3]The extrapolations in this paragraph are all based on the (green) variational update energies. For the simple and full update points we can use the same procedure.

than our $D = 10$ simple update energy. Note that the ground state energy per site of the SU(3) Heisenberg model is related to the ground state energy per site of the BBH model at $\theta = \pi/4$ through $E_{\mathrm{BBH}}(\pi/4) = \frac{1}{\sqrt{2}}\left(E_{\mathrm{SU(3)}} + 3\right)$; see Section 4.A.1 for details.

4.5 iPEPS results

4.5.1 Simple update results

To obtain a rough picture of the phase diagram, we have performed randomly initialized simple update simulations for unit cells up to size 6x6 and bond dimensions $D = 1, 2, 3, \ldots, 8$ for 80 equidistantly spaced values of $\theta \in [0, 2\pi)$. The resulting energy per site as a function of θ is shown in Fig. 4.4 (top). For each fixed value of θ, only the lowest energy of all unit cells considered is shown.

Observing the average magnetization and Q-norm per site displayed in the middle and bottom graphs of Fig. 4.4, the simple update simulations show four different phases. Starting at $\theta = 0$, we have, in order of increasing θ, the 120° magnetically ordered (AFM3), antiferroquadrupolar (AFQ), ferromagnetic (FM) and ferroquadrupolar (FQ) phases, with transitions occurring at $\theta = \pi/4$, $\pi/2$, $5\pi/4$ and roughly 1.9π respectively. The simple update results quantitatively agree with the phase diagram found by Läuchli et al. [155]. Moreover, the jumps in the magnetization suggest that the corresponding phase transitions are of first order.

The simple update results do not hint at the existence of any phases other than those occurring in the product state phase diagram. However, we have learned from our study of the corresponding square lattice model that—close to transition points especially—randomly initialized simple update simulations can overlook certain phases. Therefore, we will next proceed with a more thorough full and variational update analysis, and investigate all four of the above phase transitions. In particular, we will have a look at the FQ to AFM3 transition, and provide a more accurate estimate of the critical value of θ for which the transition occurs. Note that the locations of the other three transitions are fixed, either because they sit at one of the SU(3)-symmetric points $\theta = \pi/4$ and $5\pi/4$, or because the extent ($\pi/2 < \theta < 5\pi/4$) of the FM product state phase is independent of the underlying two-dimensional lattice structure. Additionally, we will keep an eye out for a possible appearance of the $m = 2/3$ phase, as well as determine the extent of the one-dimensional Haldane phase in the anisotropic triangular lattice spin-1 BBH model.

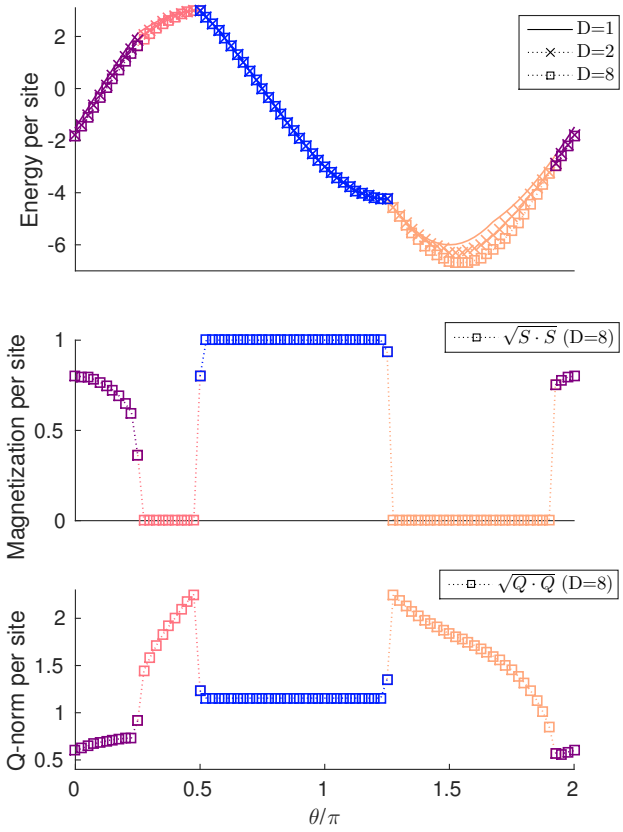

Figure 4.4: *Energy,* (top)*, magnetization* $m = \sqrt{\boldsymbol{S} \cdot \boldsymbol{S}}$ (middle) *and Q-norm* $\sqrt{\boldsymbol{Q} \cdot \boldsymbol{Q}}$ (bottom) *per site for randomly initialized simple update simulations. From left to right we have the AFM3, AFQ, FM and FQ phases (color online). The magnetic phases can be recognized by a non-zero magnetization and a smaller Q-norm than that of neighboring quadrupolar phases.*

4.5.2 FQ to AFM3 transition

Making use of hysteresis in the vicinity of a first order transition, we can simulate states in the FQ and AFM3 phases just beyond the transition point by initializing them from a state that lies deeper in the phase we want to simulate. Doing so around the simple-update-estimated transition point $\theta \approx 1.9\pi$ yields the energy per site for simulations in the FQ and AFM3 phase as shown in Fig. 4.5.

For states in the FQ phase, we have imposed U(1) symmetry (aligning the on-site magnetic dipole vector along the z-axis), allowing us to push the full update to $D = 11$. The AFM3 states, however, break U(1) symmetry because the spins do

not align along a given axis, and we can therefore go up to $D = 9$ at best[4].

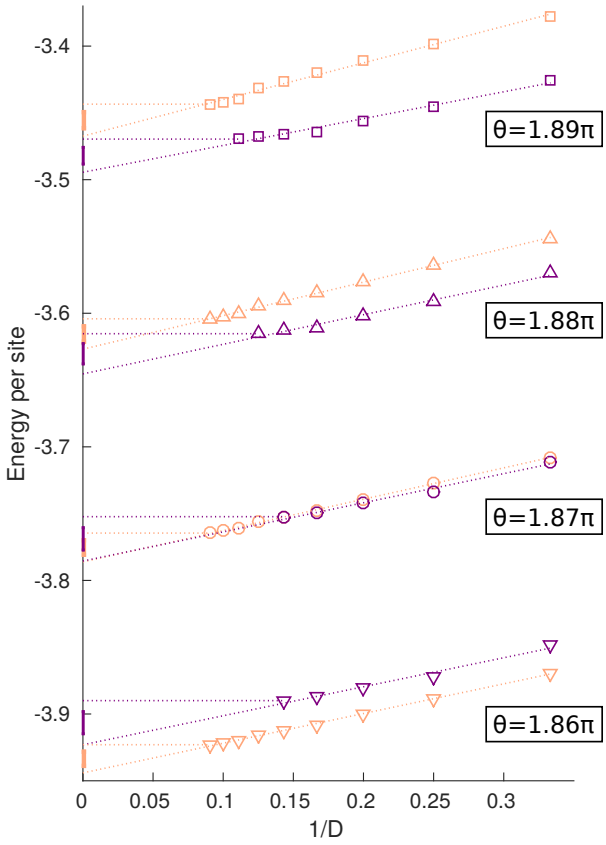

Figure 4.5: *Energy per site (full update) for FQ and AFM3 (color online) states at $\theta = 1.86\pi - 1.89\pi$ in the vicinity of the FQ to AFM3 phase transition.*

Extrapolating $D \to \infty$ as explained in Section 4.4 yields an estimated energy per site and corresponding error bar for both the FQ and AFM3 simulations at

[4]The reason that the AFM3 data points for $D = 8$ and $D = 9$ at $\theta = 1.86\pi$ and 1.87π and $D = 9$ at $\theta = 1.88\pi$ are left out is because the corresponding simulations mixed with a ferro-quadrupolar state (decreasing their magnetization significantly) during the optimization process, and are therefore not proper AFM3 simulations. Note that this does not happen the other way around because the imposed U(1) symmetry used for the FQ simulations is incompatible with the 120° magnetic order in the AFM3 phase. Regardless, the phase transition is clearly visible with the data points available.

different values of θ. Plotting the upper and lower bounds of the error bars as a function of θ (top Fig. 4.6) then gives an estimate for the critical value of θ that separates the FQ and AFM3 phases of $\theta_c = 1.873(7)\pi$. This result is a more accurate refinement of the exact diagonalization result extrapolated to infinite system size ($\theta_c^{ED} \approx 1.89\pi$) obtained by Läuchli et al. [155].

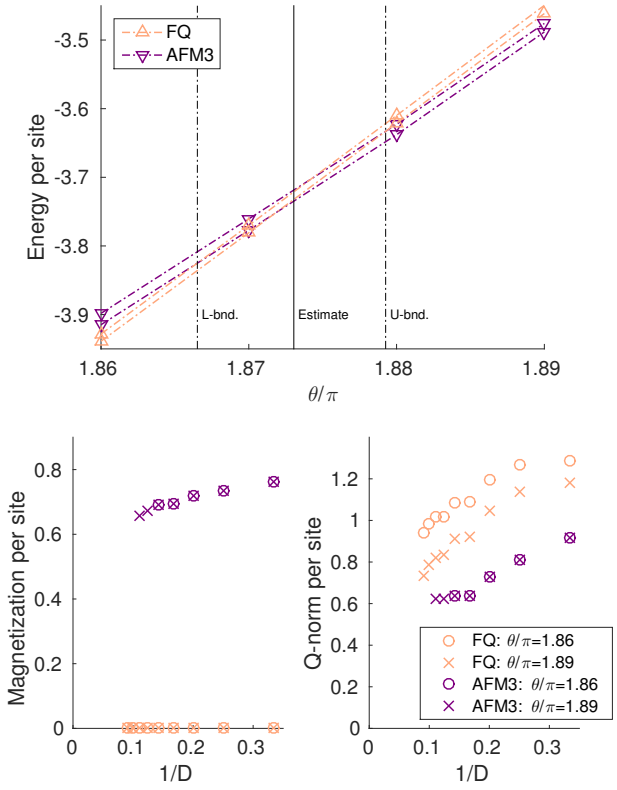

Figure 4.6: Top*: extrapolated energy per site (top and bottom of error bars from Fig. 4.5 shown) for the FQ and AFM3 states around the FQ to AFM3 phase transition. The vertical lines signified with "L-bnd." and "U-bnd." indicate the locations for which the error bars separate. The "Estimate" is the intersection point of the curves drawn through the centers of the error bars shown in Fig. 4.5. We conclude that the phase transition occurs at* $\theta_c = 1.873(7)\pi$. Bottom*: Magnetization and Q-norm per site for FQ and AFM3 states left (*$\theta = 1.86\pi$*) and right (*$\theta = 1.89\pi$*) of the phase transition. The magnetization especially displays a clear jump when going from the FQ to AFM3 phase, which, combined with the slight kink in the energy demonstrates that this transition is first order.*

The fact that the energy per site curves for the FQ and AFM3 simulations have (slightly) different slopes in Fig. 4.6 implies that the energy per site of the ground

state displays (a slight) kink at the FQ to AFM3 intersection. Supplemented by the jump in magnetization and the different $1/D$ behavior of the quadrupole norm—displayed in the bottom plots of Fig. 4.6—we can conclude that the FQ to AFM3 transition is first order.

4.5.3 AFQ to FM transition and absence of m=2/3 phase

The $m = 2/3$ magnetization plateau in the AFQ phase found by Läuchli et al. [155] at finite magnetic field (mentioned in Section 4.3) corresponds to a three-sublattice state with magnetic moments ferromagnetically aligned on two of the sublattices, and on the third a quadrupolar director parallel to the magnetic moments on the neighboring sites (Fig. 4.7). Läuchli et al. discovered that, as θ increases towards $\pi/2$, the value of the external magnetic field for which the transition to the $m = 2/3$ phase occurs decreases as θ increases, up to the critical point $\theta = \pi/2$ where the AFQ and $m = 2/3$ states are simultaneous ground states of the zero-external-field BBH model. On the square lattice, Tóth et al. [158] showed that a very similar phenomenon occurs (in that case, the partially magnetized state was half magnetized instead of two-thirds). Thus, in light of our discovery of the half-magnetized phase actually taking up a non-negligible portion of the square lattice zero-field phase diagram, it seems natural to ask whether the $m = 2/3$ phase also occurs on the triangular lattice BBH model with zero external field.

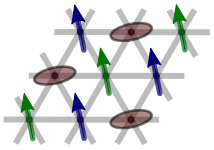

Figure 4.7: *The three-sublattice $m = 2/3$ state with ferromagnetically aligned magnetic moments on two sublattices and a director—i.e. a normal vector to the plane of fluctuations—on the third sublattice that is parallel to the neighboring magnetic moments.*

We initialized several simulations in the vicinity of $\theta = \pi/2$. The energy per site of the AFQ, FM and $m = 2/3$ simulations is shown in Fig. 4.8. We can conclude that, contrary to the square lattice case, the $m = 2/3$ states are everywhere higher in energy than the AFQ states—except at the AFQ to FM transition point where the ground state is degenerate and the $m = 2/3$ state is one of the many ground states—and thus the $m = 2/3$ phase does not occur in the zero-field phase diagram.

Note that, in the FM phase the ground state is a product state. In the vicinity of the FM phase, the ground state is very close to a product state, as can be seen from the fact that the energy does not visibly improve with increasing bond

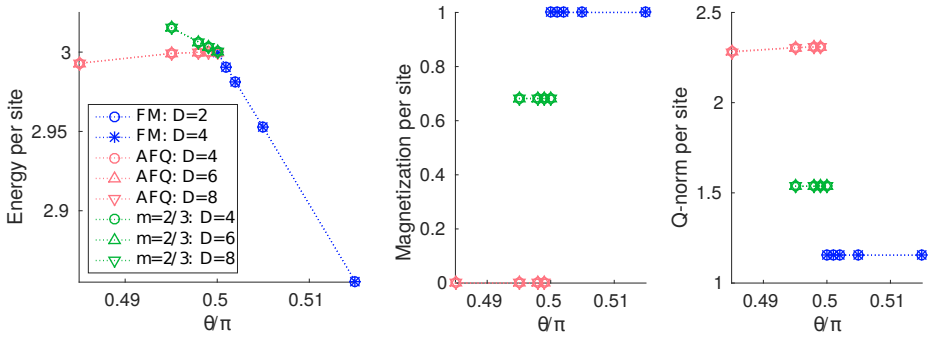

Figure 4.8: Left: *energy per site (full update) for AFQ, FM and $m = 2/3$ states around $\theta = \pi/2$. Because all states are (practically) product states, the energies do not depend on D.* Middle and right: *Magnetization and Q-norm per site (full update) for AFQ, FM and $m = 2/3$ states around $\theta = \pi/2$. The jumps in both and kink in the energy show that the transition is first order.*

dimension. Therefore, we do not have to do $D \to \infty$ extrapolations to get accurate results.

From the clear kink in the energy per site, and the jumps in magnetization and Q-norm (Fig. 4.8), we can conclude that the AFQ to FM transition is also of first order.

Finally, let us have a look at the remaining two phase transitions, located at the SU(3)-symmetric points $\theta = \pi/4$ and $\theta = 5\pi/4$. The results we find agree with previous studies, and will be presented for completeness.

4.5.4 AFM3 to AFQ transition

Approaching the phase transition at the SU(3) point $\theta = \pi/4$ from both the AFM3 and AFQ sides by slowly walking towards the critical point, loading each simulation from the last (for fixed D), we obtain the energy per site plot shown in Fig. 4.9.

Moving towards the transition as described above, we can ensure that simulations stay in their respective phases even at the critical point itself (where both $D \to \infty$ extrapolated AFM3 and AFQ states are ground states of the system). Fig. 4.9 shows the resulting magnetization and Q-norm exactly at the transition at $\theta = \pi/4$. The subtle kink in the fixed-D energy per site plots and the jumps in magnetization and Q-norm show that the transition is first order.

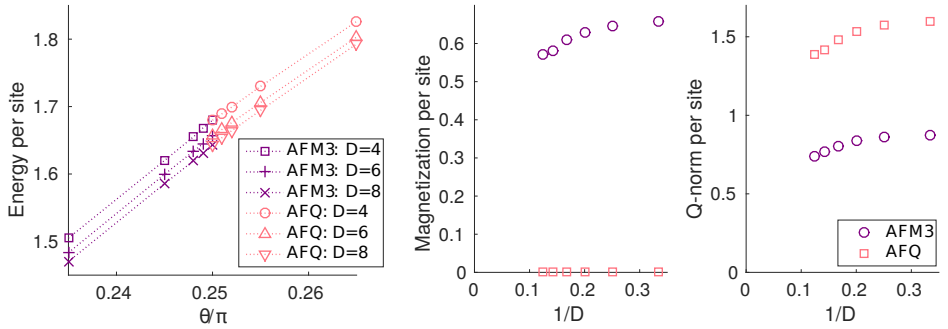

Figure 4.9: Left*: energy per site (full update) for $D = 4$, 6 and 8 for AFM3 and AFQ states around $\theta = \pi/4$.* Middle and right*: Magnetization and Q-norm per site (full update) for AFM3 and AFQ states exactly at $\theta = \pi/4$. The jumps in both and slight kink in the energy for fixed values of D show that the AFM3 to AFQ transition is of first order.*

4.5.5 FM to FQ transition

The FM to FQ phase transition can be investigated in the same manner as the AFQ to FM transition. As noted by Völl et al. [192], the ground state in (and close to) the FM phase is a product (or almost product) state, implying that no $D \to \infty$ extrapolation will be required.

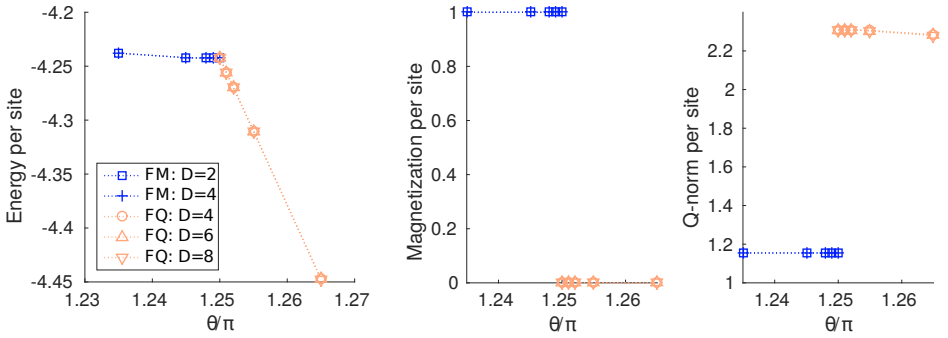

Figure 4.10: Left*: energy per site (full update) for FM and FQ states around $\theta = 5\pi/4$. The FM states are product states, and the FQ states are close to being product states as can be seen from the fact that the energies do not improve with D.* Middle and right*: Magnetization and Q-norm per site (full update) for FM and FQ states around $\theta = 5\pi/4$. The jumps in magnetization and Q-norm and the kink in the energy support the claim that this transition is first order.*

The clear kink in the energy per site and jumps in magnetization and Q-norm (Fig. 4.10) show that the FM to FQ phase transition is also of first order.

4.5.6 Haldane phase in the anisotropic model

Our previous investigation of the square lattice BBH model showed that in between the ordinary antiferromagnetic and the 120° magnetically ordered phases a quantum paramagnetic phase arises that can be adiabatically connected to the Haldane phase of decoupled one-dimensional spin-1 BBH chains. On the triangular lattice, there is no competition between two and three-sublattice order. Nevertheless, the fact that the FQ to AFM3 product ground state phase transition point at $\theta = \arctan(-2) \approx 1.658\pi$ shifts significantly to $\theta = 1.873(7)\pi$ shows that quantum fluctuations play an important role in the FQ to AFM3 transition, and perhaps also allow for the possibility of an intermediate quantum paramagnetic phase.

The first sign that hinted at the presence of a quantum paramagnetic phase on the square lattice was the vanishing magnetization in the antiferromagnetic phase. Looking at Fig. 4.6, the magnetization in the AFM3 phase clearly does not vanish in the $D \to \infty$ limit, but we do observe that the quadrupolar order of the FQ simulation at $\theta = 1.89\pi$ goes down as D increases. However, it would be too strong a claim to say that it extrapolates to zero. Besides, $\theta = 1.89\pi$ is already in the AFM3 phase, as the extrapolated FQ energy is higher than the extrapolated AFM3 energy. Thus, based on the full update results in Fig. 4.6, there is no intermediate paramagnetic phase in between the FQ and AFM3 phases.

It is possible that the FQ to AFM3 transition is not the right place to look for a paramagnetic ground state. Motivated by the emergence of the one-dimensional Haldane phase on the two-dimensional square lattice, a natural starting point for looking for a quantum paramagnetic phase is to investigate the extent of the Haldane phase on the anisotropic triangular lattice. Because the one-dimensional spin-1 BBH chain lies in the Haldane phase for $-\pi/4 < \theta < \pi/4$, this is the parameter range will shall focus on.

We introduce an additional coupling parameter $0 \leq J_{\text{anis}} \leq 1$ that modifies the diagonal and vertical bonds of the triangular lattice simultaneously; $J_{\text{anis}} = 0$ corresponding to the limit of decoupled horizontal one-dimensional chains, and $J_{\text{anis}} = 1$ corresponding to the isotropic two-dimensional triangular lattice.

To map the entire θ-J_{anis} phase diagram using full updates and $D \to \infty$ extrapolation is computationally too expensive. Thus, we shall revert to a fixed $D = 9$ simple update investigation. The result is plotted in Fig. 4.11. Note that we also looked for additional phases other than the FQ, AFM3 and Haldane phases—by running simulations with randomly initialized tensors scattered throughout the θ-J_{anis} plane—but we did not encounter other types of order.

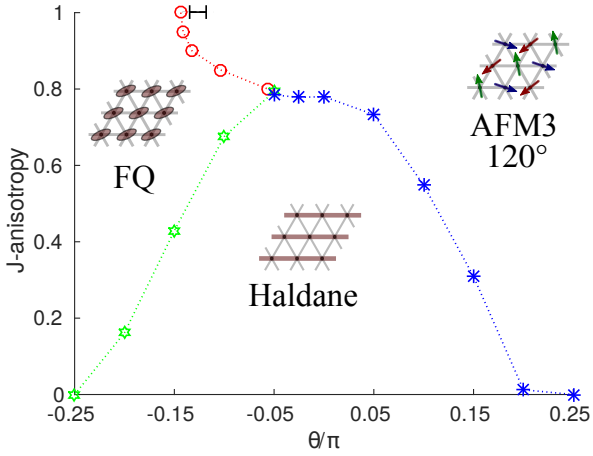

Figure 4.11: *$D = 9$ simple update phase diagram of the spin-1 BBH model on the anisotropic triangular lattice. The full update result $\theta_c = 1.873(7)\pi$ for the location of the FQ to AFM3 phase transition at $J_{\text{anis}} = 1$ indicated by the black error bar is shown to give an idea of the accuracy of the $D = 9$ simple update phase diagram.*

To estimate of the accuracy of the simple update result, we can use the FQ to AFM3 transition point at $J_{\text{anis}} = 1$ computed in Section 4.5.2. Because the critical θ_c^{simple} separating the FQ and AFM3 phases predicted by the fixed $D = 9$ simple update lies just outside the error bar of the full update result $\theta_c = 1.873(7)\pi$, we can expect that the true phase separation lines lie in the vicinity of those shown in Fig. 4.11, but their precise location cannot be inferred form the plot. However, the $D = 9$ simple update phase diagram does seem accurate enough to conclude that the Haldane phase does *not* extend all the way up to the isotropic limit.

From Fig. 4.11 we observe that the Haldane phase extends maximally in the vicinity of the Heisenberg point $\theta = 0$ (where the biquadratic coupling is zero) rather than at the FQ to AFM3 transition point. As an extra check, we have pushed our simulations at the Heisenberg point to high D (Appendix 4.A, Fig. 4.12) to verify that the magnetization stays non-zero in the $D \to \infty$ limit. In addition, we have also done full update simulations for $J_{\text{anis}} = 1$ initialized directly from within the Haldane phase and compared the energy to that of the FQ and AFM3 simulations (both close to the FQ to AFM3 transition—Appendix 4.A, Fig. 4.13, and at the Heisenberg point—Appendix 4.A, Fig. 4.14); the result of which shows that clearly, the Haldane simulations are much higher in energy in the isotropic model.

We note that the Haldane phase in the extreme anisotropic limit might a priori be better approximated by an anisotropic iPEPS (with a larger bond dimension in the

x-direction). However, by comparing the weights on the x and y-bonds obtained in the simple update approach [117] in the Haldane phase at large D, we observe that, as J_{anis} increases, the smallest weights on the x and y-bonds become of similar magnitude[5], showing that an isotropic ansatz is appropriate here. (An isotropic ansatz was also used in Chapter 3 to determine the phase boundary between the Haldane and antiferromagnetic phases on the square lattice spin-1 BBH model, but even in the strongly anisotropic limit, the iPEPS result was found to be very close to the reference value from Quantum Monte Carlo.)

Combining our results from the simple update anisotropic phase diagram, the full update study at the Heisenberg point and the full update Haldane simulations at the isotropic limit, we can safely conclude that the Haldane phase does *not* extend all the way up to the isotropic triangular lattice $J_{\text{anis}} = 1$. Moreover, we did not encounter any other signs that hint at the presence of a quantum paramagnetic phase, and we can therefore conclude that the phase diagram as shown in Fig. 4.1 is the complete ground state phase diagram.

4.6 Conclusion

We have presented a complete and systematic iPEPS study of the ground state phase diagram of the spin-1 bilinear-biquadratic Heisenberg (BBH) model on the triangular lattice. We found the ferromagnetic and 120° magnetically ordered as well as the ferro and antiferroquadrupolar phases, and precisely determined that the ferroquadrupolar to 120° magnetically ordered phase transition occurs at $\theta_c = 1.873(7)\pi$. This number is close to the exact diagonalization estimate by Läuchli et al. [155] that predicted the transition to occur at $\theta_c^{\text{ED}} \approx 1.89\pi$. Moreover, our simulations show that the partially magnetic partially nematic phase that we encountered on the square lattice does not appear on the triangular lattice spin-1 BBH model (Fig. 4.8).

Inspired by our finding of the one-dimensional Haldane phase extending all the way to the two-dimensional isotropic limit on the square lattice, we searched for signs of a possible quantum paramagnetic phase on the triangular lattice. The simple update results (Fig. 4.4) did not hint at the presence of a quantum paramagnetic phase. At the ferroquadrupolar to 120° magnetically ordered phase transition, we observed that the Q-norm of the ferroquadrupolar simulations decreases as we approach the magnetic phase (Fig. 4.6), but it still extrapolates to a non-zero number even beyond the phase transition (at $\theta = 1.89\pi$) in the magnetically ordered phase.

We then investigated the extent of the Haldane phase on the anisotropic triangular lattice (Fig. 4.11) and found that, close to the Heisenberg point $\theta = 0$, it extends

[5] There remains a difference in weights in x and y-bonds, but it shows mainly in the larger weights, not in the ones that are close to those being truncated.

maximally to approximately $J_{\text{anis}} \approx 0.8$. However, both the high D full update simulations at the Heisenberg point as well as the full update simulations initialized directly from within the Haldane phase (Appendix 4.A) confirm that the ground state is ordered, reaffirming that the ground state phase diagram of the triangular lattice spin-1 BBH model is as depicted in Fig. 4.1, and in particular does not contain a quantum paramagnetic phase. Surprisingly then, for the spin-1 BBH model, quantum effects seem to have less surprising consequences on the (in the AFM phase) geometrically frustrated triangular lattice than they do on the square lattice.

However, our study of the anisotropic model does reveal that spin-1 materials with a triangular lattice structure that are effectively described by even a simple Heisenberg antiferromagnetic coupling ($\theta = 0$) are quite sensitive to anisotropies. Indeed, we expect a transition to the Haldane phase at around $J_{\text{anis}}^{\text{triang}} \approx 0.8$, which is significantly larger than the value of $J_{\text{anis}}^{\text{square}} \approx 0.04$ for which the same transition occurs at the Heisenberg point on the square lattice. This fact could possibly be used for future experimental research that attempts to realize the extended Haldane phase in an actual two-dimensional material.

From the perspective of tensor network methods—viewing the triangular lattice as a square lattice with additional diagonal next-nearest neighbor interactions—we would like to point out that this is one of the few systematic full update studies of models beyond nearest-neighbor interactions (see also Refs. [70, 75, 130, 176, 193]).

Lastly, having accurately established the ground state phase diagram of the triangular lattice spin-1 BBH model in the thermodynamic limit by means of an unbiased method, future research can more confidently look at exited states or additions to the Hamiltonian beyond the biquadratic interaction in search of an explanation of the unusual behavior of $NiGa_2S_4$ [154, 156, 157, 161, 178–181] and the $6H$-B phase of $Ba_3NiSb_2O_9$ [159, 162, 163, 182, 183].

4.A Appendix

4.A.1 Energy comparison at the SU(3) point

The extrapolated ground state energy found by Bauer et al. [169] for the SU(3) Heisenberg model defined by the triangular-lattice nearest-neighbor Hamiltonian

$$H_{\mathrm{SU}(3)} = \sum_{\langle i,j\rangle} P_{ij},$$

where P_{ij} permutes the states of sites i and j, is: $E_{\mathrm{SU}(3)} = -0.69(2)$ $(J = 1)$. We want to compare the energy per site of the SU(3) Heisenberg model to the energy per site of the spin-1 BBH model at $\theta = \pi/4$.

In order make this comparison, let us explictly assume a finite system of N sites and compare the Hamiltonians for both systems. Moreover, we will need

$$\boldsymbol{S}_i \cdot \boldsymbol{S}_j + \boldsymbol{Q}_i \cdot \boldsymbol{Q}_j = 2P_{i,j} - \frac{2}{3} \tag{4.3}$$

(see Penc and Läuchli [170]). Now, including the θ-dependent constant that we left out in the main text of this chapter, we have:

$$\begin{aligned} H_{\mathrm{BBH}}(\theta) &= \sum_{\langle i,j\rangle} \cos(\theta)\boldsymbol{S}_i \cdot \boldsymbol{S}_j + \sin(\theta)\left(\boldsymbol{S}_j \cdot \boldsymbol{S}_j\right)^2 \\ &= \sum_{\langle i,j\rangle} \Bigg(\left[\cos(\theta) - \frac{\sin(\theta)}{2}\right] \boldsymbol{S}_i \cdot \boldsymbol{S}_j \\ &\qquad + \frac{\sin(\theta)}{2}\left(\boldsymbol{Q}_j \cdot \boldsymbol{Q}_j\right)^2 + \frac{4}{3}\sin(\theta)\Bigg), \end{aligned}$$

which, at $\theta = \pi/4$ equals,

$$\begin{aligned} H_{\mathrm{BBH}}(\pi/4) &= \sum_{\langle i,j\rangle} \left(\frac{1}{2\sqrt{2}} \left[\boldsymbol{S}_j \cdot \boldsymbol{S}_j + \boldsymbol{Q}_j \cdot \boldsymbol{Q}_j\right] + \frac{4}{3\sqrt{2}} \right) \\ &= \sum_{\langle i,j\rangle} \left(\frac{1}{\sqrt{2}} P_{i,j} + \frac{1}{\sqrt{2}} \right) \\ &= \frac{1}{\sqrt{2}} \sum_{\langle i,j\rangle} P_{i,j} + \frac{3N}{\sqrt{2}} \\ &= \frac{1}{\sqrt{2}} H_{\mathrm{SU}(3)} + \frac{3N}{\sqrt{2}} \end{aligned}$$

where we've used (4.3) to go to the second line, and the fact that the triangular lattice has a coordination number of 6 (hence 6N/2 terms in the sum) to go to the third.

Finally, when relating energies per site, we have to divide the equation by the number of particles N, yielding the following ground state energy per site relation

$$E_{\mathrm{BBH}}(\pi/4) = \frac{1}{\sqrt{2}}\left(E_{\mathrm{SU(3)}} + 3\right). \tag{4.4}$$

Thus, by (4.4), $E_{\mathrm{SU(3)}} = -0.69(2)$ corresponds to $E_{\mathrm{BBH}} = 1.633 \pm 0.014$ (keeping one extra digit since rounding off to 1.63 ± 0.01 yields an incorrect upper bound).

4.A.2 The Heisenberg point

We have looked for signs of a vanishing magnetization at the Heisenberg point ($\theta = 0$)—a point that lies in the region where the Haldane phase extends furthest in the θ-J_{anis} phase diagram towards the isotropic limit (Fig. 4.11)—by pushing the simple update to $D = 11$, and the full and variational update to $D = 9$. The resulting energy, magnetization and Q-norm per site are plotted in Fig. 4.12.

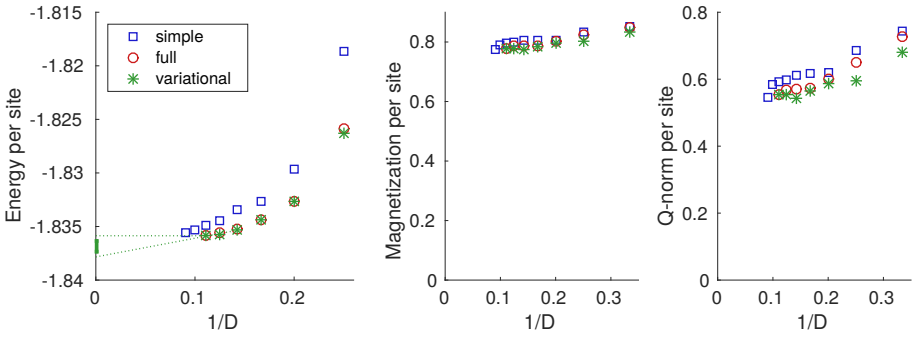

Figure 4.12: *Energy (*left*), magnetization (*middle*) and Q-norm (*right*) per site for the simple, full and variational update algorithm at the Heisenberg point $\theta = 0$. The variational update results extrapolate to a ground state energy of $E^{\mathrm{var}}_{D\to\infty} = -1.8368(5)$.*

The full and variational update simulations (Fig. 4.12) clearly extrapolate to a finite magnetic and quadrupole moment, and we can therefore conclude that the ground state is ordered at $\theta = 0$. The less-accurate simple update magnetization and Q-norm seem to curve downwards, but this is likely an artifact of the simple update, as the $D = 11$ simple update result is very similar in energy, magnetization and quadrupole moment to the $D = 8$ full and variational update results.

Moreover, magnetization and quadrupole curves as a function of $1/D$ typically do not lie on a perfectly straight line, so not too much importance should be given to an individual data point.

4.A.3 Haldane simulations at the isotropic limit

As a final check, we have initialized full update simulations from within the Haldane phase directly at the isotropic limit $J_{\text{anis}} = 1$ at two points of interest.

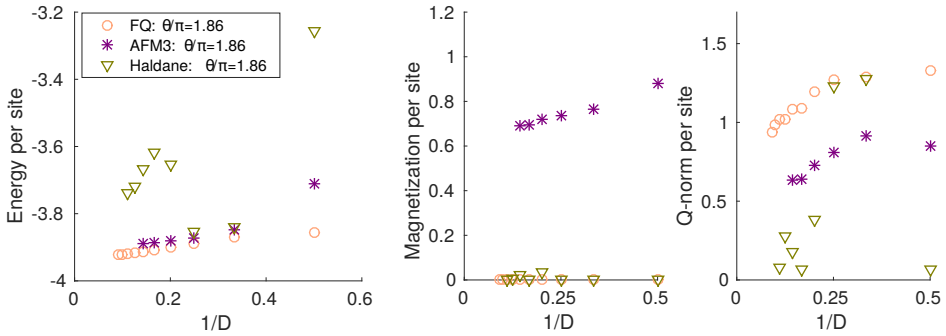

Figure 4.13: *Energy* (left)*, magnetization* (middle) *and Q-norm* (right) *per site (full update) comparing the FQ and AFM3 simulations to simulations initialized in the Haldane phase at* $\theta = 1.86\pi$*. The fluctuations in both order parameters show that the Haldane-initialzed simulations do not stay in their original phase.*

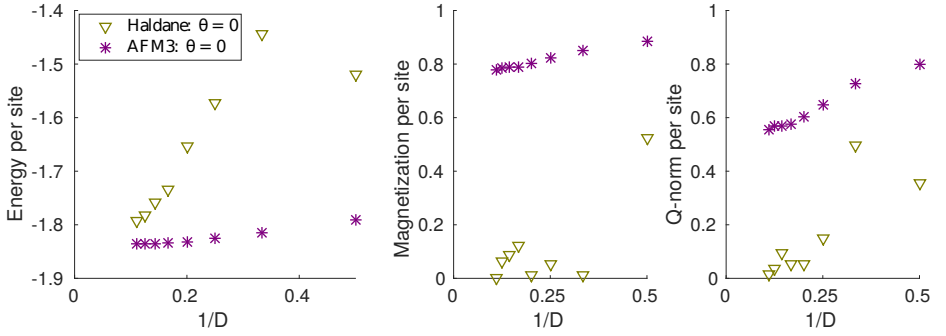

Figure 4.14: *Energy* (left)*, magnetization* (middle) *and Q-norm* (right) *per site (full update) comparing the AFM3 simulations to simulations initialized in the Haldane phase at the Heisenberg point* $\theta = 0$*. Also here, the fluctuations in both order parameters show that the Haldane-initialized simulations do not stay in their original phase.*

Close to the FQ to AFM3 phase transition—at $\theta = 1.86\pi$—Fig. 4.13 (left) shows that the simulations initialized in the Haldane phase are far from competitive, with the exception of the $D = 3$ and $D = 4$ simulations. However, Fig. 4.13 (middle and right) reveal that the aforementioned simulations are actually in the FQ phase, as their quadrupole moment shows. The other Haldane-initialized simulations also develop some quadrupolar order in the energy-minimization process, supporting the claim that the ground state is quadrupolar. Note that it therefore also does not make sense to do a $D \to \infty$ extrapolation on the Haldane-initialized simulations, as the simulations are not in a well-defined phase.

At the Heisenberg point $\theta = 0$, we encounter a similar situation. Also in this case, the energy of the Haldane-initialized simulations is far from competitive. Moreover, the Haldane-initialized simulations do not remain paramagnetic in the optimization process because they develop magnetic and quadrupolar order (Fig. 4.14). Thus, as before, it does not make sense to do a $D \to \infty$ extrapolation on the Haldane-initialized simulations.

In conclusion: the ground state is ordered at both $\theta = 1.86\pi$ and $\theta = 0$, and the Haldane phase is absent in the isotropic limit.